

Solvation Structure and Mobility Mechanism of OH[−]: A Car–Parrinello Molecular Dynamics Investigation of Alkaline Solutions

Bin Chen,^{*,†} Ivaylo Ivanov,[‡] Jung Mee Park,[‡] Michele Parrinello,^{§,||} and Michael L. Klein[†]

Center for Molecular Modeling and Department of Chemistry, University of Pennsylvania, 231 S. 34th Street, Philadelphia, Pennsylvania 19104-6323, Department of Chemistry, Division of Molecular and Life Science, Pohang University of Science and Technology, San 31, Hyojadong, Namgu, Pohang 790-784, Korea, Centro Svizzero di Calcolo Scientifico (CSCS), via Cantonale, 6928 Manno, Switzerland, Physical Chemistry, ETH Zurich, Hönggerberg, 8093 Zurich, Switzerland

Received: July 11, 2002; In Final Form: September 10, 2002

The hydroxide ion (OH[−]) has an unusually high mobility in water, comparable to that of the proton. However, a consensus view of the OH[−] mobility mechanism and its solvation structure has yet to emerge. In addition, X-ray and spectroscopic experiments reveal significant changes in the structural and dynamical properties of water in the presence of OH[−]. To gain insight into these questions, we have carried out Car–Parrinello molecular dynamics (CPMD) calculations for aqueous NaOH and KOH solutions under ambient conditions over a wide range of concentrations. These simulations are able to reproduce many puzzling phenomena, in particular, the loss of tetrahedral coordination of water (interpreted from a recent neutron diffraction with isotopic substitution experiment) and the appearance of new spectroscopic features at high concentrations. Furthermore, it is demonstrated that the observed behavior is a result of the formation of a variety of compact hydroxide–water complexes. The distribution of these complexes is dependent upon the concentration and the counterion. The present results reconcile conflicting structural interpretations from previous experimental and theoretical studies on hydroxide solutions. Analysis of the CPMD trajectories supports the view that the transport mechanism of the hydroxide ion is distinct from that of the proton.

1. Introduction

Both the proton and the hydroxide ion (OH[−]) have unusually high mobilities in water. While extensive investigations^{1–7} have given rise to a common view of the mobility mechanism of the proton, relatively little work has been carried out to understand the mechanism for hydroxide.^{1,8–11} It was generally believed that the mobility mechanism of the latter may resemble that of the proton since they have similar mobilities¹² and the hydroxide ion can be viewed as a water molecule with a missing proton or a “proton hole”.^{13,14} However, this belief was recently challenged by an ab initio CPMD calculation by Tuckerman et al. for a system with 1 OH[−] in 31 H₂O,^{1,11} in which they found that the hydroxide ion has its own unique mobility mechanism.

The mobility mechanism is inextricably linked to the solvation structure. However, a variety of solvated hydroxide complexes were suggested in previous experimental and theoretical studies (see Figure 1).^{1,11,12,14–20} Gas-phase mass spectrometric measurements pointed to a shell closure at three water molecules.¹⁵ This was interpreted by Agmon¹² as either H₇O₄[−] (three water molecules coordinated directly with OH[−] through hydrogen-bonds) or H₃O₂[−] with two additional water molecules hydrogen bonded to the two oxygen atoms. On the contrary, spectroscopic experiments on concentrated solutions suggested that H₃O₂[−] is the dominant solvation structure.^{16–20} However, both findings are not supported by the ab initio study by Tuckerman et al. on an aqueous system with 1 OH[−] and 31 H₂O in periodic boundary

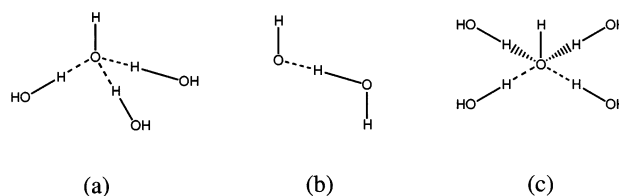


Figure 1. Schematic drawings of the solvation structure of OH[−] interpreted from gas-phase mass spectrometric measurements (a and b),^{12,15} spectroscopic experiments on concentrated hydroxide solutions (b),^{16–20} the ab initio study of 1 OH[−] in 31 water (c),^{1,11} and the ab initio calculation on gas-phase hydroxide–water clusters (a).^{22,23}

conditions and no counterion.^{1,11} Instead, a new complex, H₉O₅[−], was reported to be the dominant solvation structure for OH[−], in which four water molecules are coordinated with OH[−] through hydrogen-bonding in a roughly planar conformation. This is consistent with a high solvation number between 5 and 6 for OH[−], as determined from a recent dielectric relaxation experiment on a dilute NaOH solution.²¹ In addition, the work by Tuckerman et al.^{1,11} indicated that H₇O₄[−] is only a transient structure and a “vehicle” for hydroxide mobility. Nevertheless, some more recent ab initio calculations on gas-phase hydroxide–water clusters suggested that H₉O₅[−] is less stable than H₇O₄[−] with one water in its second solvation shell.^{22,23}

Apart from these controversial structural issues concerning solvated OH[−], many experiments have demonstrated that the structural and dynamical properties of water undergo significant changes in the presence of OH[−]. For example, both Raman and IR spectroscopy reveal dramatic change in the vibrational spectra, particularly a broadening of the normal water OH stretch.^{16–20,24} Interestingly, at high concentrations, a “free”

* Corresponding author: binchen@cmm.chem.upenn.edu

[†] University of Pennsylvania.

[‡] Pohang University of Science and Technology.

[§] Centro Svizzero di Calcolo Scientifico.

^{||} ETH Zurich.

O–H stretch appears in the Raman spectrum but not in the IR (it was inferred from this fact that H₃O₂[−] is the dominant solvation structure²⁰). Also, in a recent neutron diffraction experiment with isotopic substitution (NDIS) on a 40 wt % NaOH solution,²⁵ it was found that the 4.4 Å peak in the OO radial distribution function (RDF) of pure water (a feature of the tetrahedral short-range coordination of water) is completely absent. In addition, the OH and HH RDFs show large shifts of the peak positions: the hydrogen bond peak position moves from 1.85 Å for pure water to 1.65 Å for the NaOH solution and the HH RDF peak positions also shift significantly to shorter distances (from 2.4 and 3.8 Å to 2.15 and 3.5 Å).

To gain insight into these problems, an extensive Car–Parrinello molecular dynamics (CPMD)²⁶ investigation was carried out on the hydroxide system (namely, aqueous NaOH and KOH solutions) under ambient conditions over a wide range of concentrations. There are a few advantages of using this first-principles approach. First, it avoids the need for empirically determined parameters and is not restricted to pairwise interaction potentials. Second, proton transfer, which is important for this system, can be modeled accurately. The results obtained can also be critically compared to those generated from the empirical valence bond approach and the QM/MM methods.^{6,7,10} The remainder of this article is arranged as follows. Section 2 gives the simulation details. The simulation results are presented in section 3, and section 4 provides concluding remarks.

2. Simulation Details

All simulations were performed with the program CPMD,²⁷ which is an implementation of the original Car–Parrinello molecular dynamics scheme,²⁶ based on density functional theory (DFT), periodic boundary conditions, plane wave basis sets, and pseudopotentials. The Becke, Lee, Yang, and Parr (BLYP) exchange correlation functional with the generalized gradient approximation^{28,29} was adopted because it has been shown to give a good description of aqueous systems.^{3,5,30–32} For all atoms, the nonlocal norm-conserving Troullier–Martins pseudopotentials³³ were used to describe the valence–core interactions. All pseudopotentials have been transformed to a fully nonlocal form using the scheme of Kleinman and Bylander.³⁴ To improve the accuracy of the results for the alkali metals and to properly account for the nonlinear exchange and correlation core effects, semicore pseudopotentials were used for Na and K.³⁰ The valence electronic wave functions were expanded in a plane wave basis set up to an energy cutoff of 70 Ry for KOH and 80 Ry for NaOH. Hydrogen nuclei were treated as classical particles with the mass of the deuterium isotope.³⁵ A fictitious electronic mass²⁶ of 500 (600) a.u. was employed for KOH (NaOH). The equations of motion were integrated with a time step of 0.121 fs. This set of parameters enabled us to maintain adiabatic conditions for the electrons over the full length of the trajectories.

Simulations were carried out for five NaOH/H₂O systems: (i) 64 H₂O (0 M); (ii) 1 NaOH in 36 H₂O (1.5 M); (iii) 3 NaOH in 36 H₂O (4.5 M); (iv) 8 NaOH in 24 H₂O (15 M); and (v) 16 NaOH in 48 H₂O (15 M) plus two KOH/H₂O systems: (vi) 1 KOH in 43 H₂O (1.3 M) and (vii) 11 KOH in 32 H₂O (14 M). It should be noted that for the most concentrated NaOH solution investigated here, 15 M, two separate simulations with different system sizes were performed to check for finite-size effects. For all systems, cubic cells with periodic boundary conditions were used with cell lengths determined from the experimental densities.³⁶ The production run consisted of 10 ps for systems i and v, and more than 30 ps for the rest. As the initial setup

and equilibration were somewhat different for the KOH and NaOH systems, they are described separately below.

For the concentrated KOH solution, an initial configuration was constructed using the ice structure^{37,38} in which 11 H atoms were selected randomly and replaced by K atoms. An NVE simulation was carried out until the system reached equilibrium at about 600 K. The system was subsequently cooled to 300 K using temperature rescaling. A Nosé–Hoover thermostat^{39–41} was applied at 300 K for 5 ps. The average classical energy was calculated for this short trajectory. Then a production run was carried out in the NVE ensemble with a classical energy close to this average value. The average nuclei temperature was 294 K.

For the diluted KOH solution, the initial configuration was generated from an equilibrated configuration of K⁺ in water taken from the simulation of Ramanian et al.³⁰ It contained 1 K⁺ ion and 59 water molecules. The potassium ion and 44 representative water molecules were chosen from this configuration, and a single OH[−] ion was created by removing a hydrogen atom from a water molecule, separated as far as possible from the K⁺ ion. A Nosé–Hoover thermostat^{39–41} was applied at 300 K for 5 ps, followed by a production run in the NVE ensemble. The average nuclei temperature was 308 K.

The simulations for NaOH were started from equilibrated NaCl configurations of corresponding concentrations obtained from classical simulation, in which each chloride ion was replaced by an OH[−]. The oxygen nucleus coincided with the position of the chloride ion, and a suitable position for the hydrogen atom was determined from the normal OH bond length and optimized with respect to the hydrogens of the neighboring water molecules. A short simulation run was performed during which the temperature was controlled by uniformly scaling the velocities to the target simulation temperature of 300 K whenever the tolerance interval of 50 K was exceeded. The system was then equilibrated at 300 K for about 2 ps using a Nosé–Hoover chain thermostat^{39–41} with a chain length of four and frequency of 2500 cm^{−1}. The production runs were carried out in the NVE ensemble using the same Nosé–Hoover chain thermostat condition.

A short preliminary report of our work has been presented elsewhere.⁴³

3. Results and Discussions

A. Radial Distribution Functions. Plotted in Figures 2 and 3 are the oxygen–oxygen (*g_{OO}*), oxygen–hydrogen (*g_{OH}*), and hydrogen–hydrogen (*g_{HH}*) radial distribution functions (RDF) calculated from the simulations. The results given by the two separate simulations with different system sizes on the 15 M NaOH solution agree well with each other. Therefore, finite-size effects are not significant for these quantities. For both NaOH and KOH solutions, it is evident that a continuous change of the water structure occurs with the increase of the salt concentration. This change is mainly characterized by a large shortening of the intermolecular separations, a small lengthening of the intramolecular separations (see *g_{OH}* and *g_{HH}* in Figure 3), and correspondingly an increasing overlap between these two.

Most noticeable is the shift of the second peak of *g_{OO}* to significantly shorter distances, from 4.4 Å for pure water (a characteristic of tetrahedral coordination) to 3.6 Å for the 15 M NaOH solution and 3.9 Å for the 14 M KOH solution. This clearly indicates a loss of the tetrahedral coordination of water in the concentrated solutions, which is in agreement with the structural interpretation from the NDIS experiment²⁵ on a 40

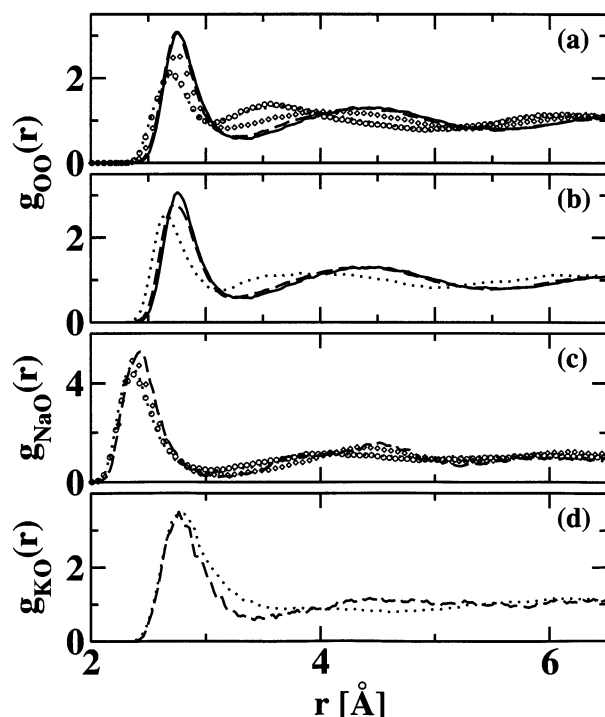


Figure 2. O–X (X is O, Na⁺, or K⁺) radial distribution functions calculated for pure water (solid line, shown in panels a and b), NaOH (shown in panels a and c) at 1.5 M (dashed line), 4.5 M (diamonds), and 15 M (dots and circles), and KOH (shown in panels b and d) at 1.3 M (dashed line) and 14 M (dotted line). In panels a and c, the circles (dots) are for the larger (smaller) of the two 15 M NaOH systems.

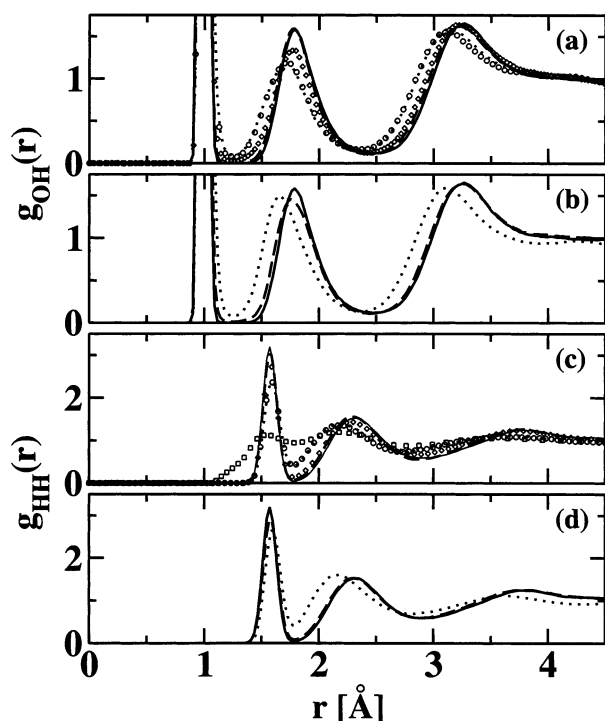


Figure 3. O–H and H–H radial distribution functions. Symbols as in Figure 2. The neutron diffraction data for a 40 wt % NaOH solution²⁵ are shown as squares in panel c.

wt % NaOH solution. Unfortunately, only H/D isotopic substitution was employed in the NDIS experiment, which allowed determination of g_{HH} but not the other RDFs and thus prevented a direct comparison of g_{OO} with experiment. Part of the structural change is contributed by Na⁺ or K⁺. The larger shift of the peak position observed in the NaOH system is likely due to the

smaller size of Na⁺, which brings the neighboring oxygens closer (see Figure 2). Compared to the second peak, the first peak shifts by a much smaller amount ≈ 0.1 Å but exhibits a more pronounced decrease in the height, by about 30% for the 15 M NaOH solution and 20% for the 14 M KOH solution. The shift of this peak to shorter distances is mainly caused by the strong hydroxide ion–water interactions, whereas the decrease of its height is due to the dilution effects from Na⁺ or K⁺ ions.

The strong hydroxide ion–water interactions are also reflected in the peak shifts of g_{OH} and g_{HH} . For example, the intramolecular peaks show a shift and a broadening to larger distances. In contrast, the intermolecular peaks shift in the opposite direction by a larger magnitude. For example, the hydrogen-bond peak position (the second peak of g_{OH}) moves from 1.8 Å for pure water to 1.7 Å for the 15 M NaOH solution and 1.65 Å for the 14 M KOH solution. A similar amount of shift is observed for the second peak of g_{HH} and the corresponding positions are 2.3, 2.2, and 2.15 Å, respectively. As a result, there is a significant overlap between the intra- and intermolecular RDFs, an indication of proton-transfer events. The NDIS experiment also reported similar shifts of these intermolecular peaks in the 40 wt % NaOH solution:²⁵ the second peak of g_{XH} (where X represents both oxygen and sodium) and g_{HH} appears at 1.65 and 2.18 Å, respectively. However, the experiment found a much more significant overlap between the intra- and intermolecular peaks (see Figure 3c). In addition, the experimental g_{HH} also show a much broader intramolecular peak with tailing to much shorter distances (up to 1 Å).

The RDF results presented above are averaged over all oxygens and/or hydrogens and do not provide a view of the local structures of individual molecular species (i.e., OH[−]) comprising the ensemble of transient solvation environments. To extract such detailed structural information about OH[−], some additional analysis was performed. First OH[−] was identified by assigning each hydrogen to its nearest neighbor oxygen (i.e., if an oxygen had only one hydrogen assigned to it, this oxygen–hydrogen pair was then an OH[−]). The OH[−] ions were further classified into different categories according to δ_{\min} ,⁴⁴ which was defined as the shortest asymmetric stretch coordinate δ ($= r_{O^*H_d} - r_{O_dH_d}$), among all the hydrogen-bond donors to (O^{*}H[−])[−] (δ_{\min} will also be used later as the proton transfer coordinate). The structural analysis was then carried out separately for the (O^{*}H[−])[−] ions with large δ_{\min} (> 0.5 Å, called type I) and small δ_{\min} (< 0.1 Å, called type II).¹¹ Whereas the large δ regime represents the case when the proton is localized on the water molecule, the small δ regime represents the special scenario when a proton is in the process of being transferred to OH[−]. Plotted in Figures 4 to 6 are the RDFs of these two types of (O^{*}H[−])[−], g_{O^*O} , g_{O^*H} , g_{HO} , and the corresponding coordination number integrals, $n(r)$.

For all systems investigated here, appreciable structural differences are present in the solution environment around these two types of OH[−]. Most prominent is the splitting of the first solvation shell around the type II OH[−] into two distinct domains (see Figures 4 and 5, two short-range intermolecular peaks appear in the g_{O^*O} and g_{O^*H}). In particular, a new region appears at a significantly shorter distance (about 2.45 Å in terms of the OO separation and 1.25 Å for the OH), compared to the normal first solvation shell separations (i.e., 2.7 Å and 1.8 Å for OO and OH, respectively). From $n(r)$, it is evident that the appearance of this new region is caused mostly by the one hydrogen-bond donor with the shortest δ . Despite the gain of this additional domain, the total coordination number actually

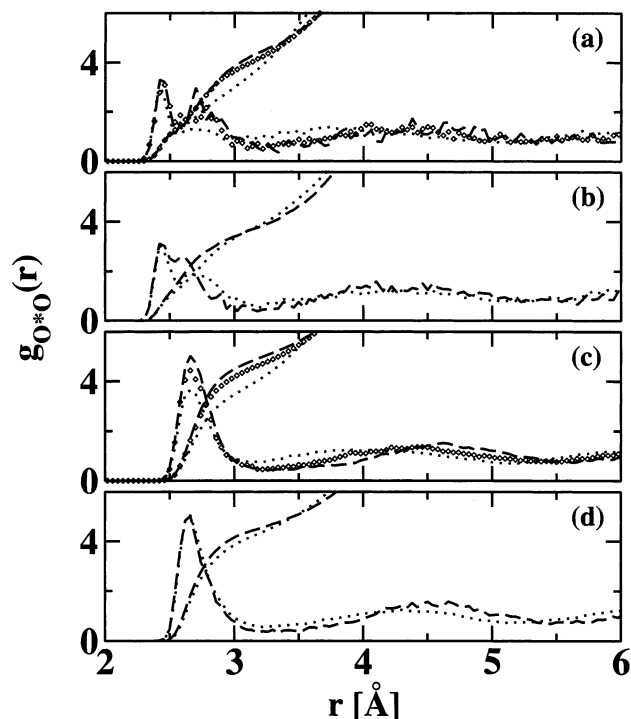


Figure 4. O*–O radial distribution functions and their corresponding number integrals calculated for O* with $\delta_{\min} < 0.1$ (panels a and b) and $\delta_{\min} > 0.5$ (panels c and d). Panels a and c are for NaOH and panels b and d are for KOH. Symbols as in Figure 2.

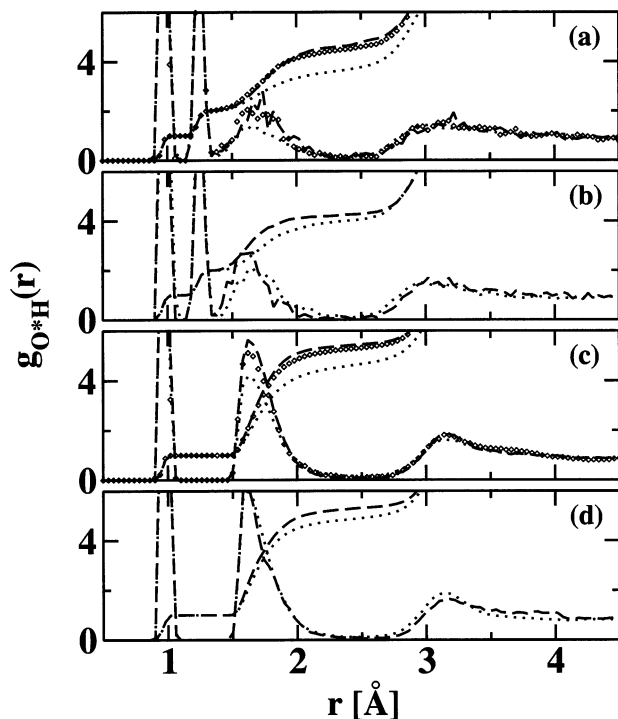


Figure 5. O*–H radial distribution functions and their corresponding number integrals calculated for O* with $\delta_{\min} < 0.1$ (panels a and b) and $\delta_{\min} > 0.5$ (panels c and d). Panels a and c are for NaOH and panels b and d are for KOH. Symbols as in Figure 2.

decreases from the type I to the type II OH⁻. For example, the O*O coordination number (up to a distance of 3.2 Å) decreases from 4.5 to 3.8 for the 1.3 M KOH solution and 4.3 to 3.9 for the 14 M KOH solution. The corresponding decrease for the NaOH solutions is: 5.0 to 4.4 for 1.5 M, 4.7 to 4.2 for 4.5 M, and 4.1 to 3.8 for 15 M. The O*H coordination number (up to

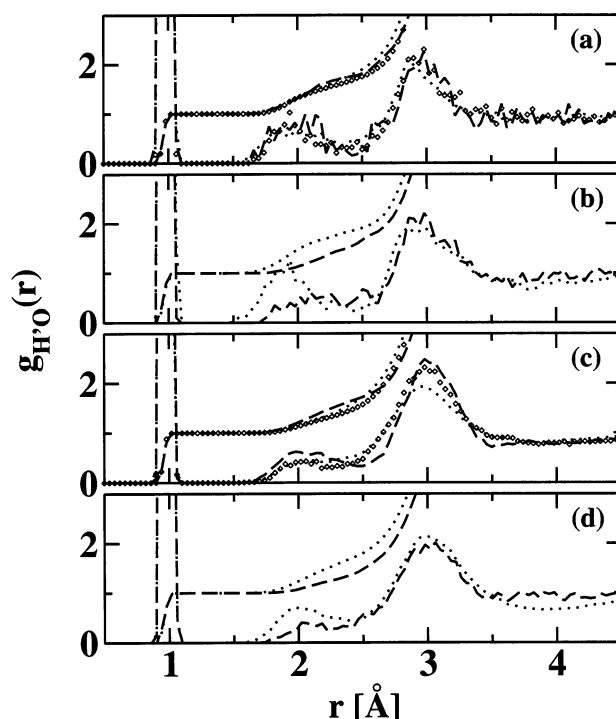


Figure 6. H'–O radial distribution functions and their corresponding number integrals calculated for H' with $\delta_{\min} < 0.1$ (panels a and b) and $\delta_{\min} > 0.5$ (panels c and d). Panels a and c are for NaOH and panels b and d are for KOH. Symbols as in Figure 2.

a distance of 2.4 Å and excluding the one bonded intramolecularly) also decreases substantially: 4.3 to 3.3 (1.3 M KOH), 3.9 to 3.0 (14 M KOH), 4.4 to 3.6 (1.5 M NaOH), 4.3 to 3.5 (4.5 M NaOH), and 3.6 to 2.7 (15 M NaOH). A decrease of nearly one hydrogen neighbor supports a relatively large solution structural reorganization around OH⁻ with the change of δ_{\min} (see also discussions later in the section on the solvation structures and proton-transfer mechanisms of OH⁻).

Comparison of the coordination numbers between these different systems demonstrates that the solution environment around OH⁻ also depends on the concentration and the counterion. In general, the increase of the concentration leads to a decrease of coordination numbers around OH⁻. This is presumably due to the sharing of the solvent water molecules between more ions at higher concentrations. At low concentrations, on average, an OH⁻ is surrounded by more water neighbors in the NaOH solutions compared to the KOH. Inspection of the configurations show that the sodium and hydroxide ions have a higher tendency to stay close to each other as a solvent separated ion pair (i.e., separated by one water molecule). The neighboring sodium ions might contribute to the increase of the number of water neighbors (also see later discussions on solvation structures). Interestingly, the opposite result was found at high concentrations. However, in this case, both K⁺ and Na⁺ have higher chances to form direct contact pairs with OH⁻. The relative size of the ion might play a role. In particular, the smaller Na⁺ ion brings OH⁻ closer and causes a larger depletion of water molecules around OH⁻.

It should be noted that the first intermolecular peak of these RDFs generally moves to shorter distances compared to pure water, which emphasizes again the strong interactions between OH⁻ and water and explains part of the observed shifts in the overall RDFs shown in Figures 2 and 3. A notable exception is $g_{H'O}$. In fact, the first intermolecular peak of $g_{H'O}$ is barely noticeable, in sharp contrast to g_{O*H} . This indicates that the

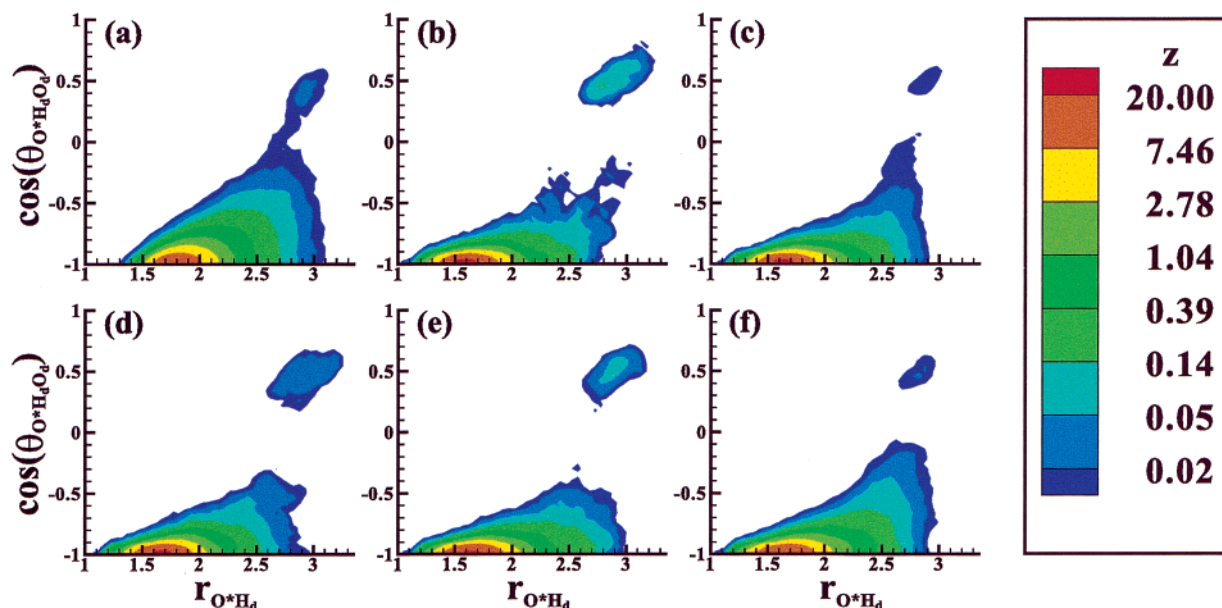


Figure 7. Contours of the two-dimensional distribution function of the O*...H_d distance and of the cosine of the O*...H_dO_d angle calculated for pure water (panel a), KOH at 1.3 M (panel b) and 14 M (panel c), NaOH at 1.5 M (panel d), 4.5 M (panel e), and 15 M (panel f).

hydrogen of OH[−] is only weakly hydrogen-bonded to other oxygens. In addition, this peak is even weaker at larger δ_{\min} . It appears slightly more visible in the 14 M KOH solution.

B. Local Structure around OH[−]. The RDFs and number integrals presented so far are radially averaged quantities and do not provide a complete view of the solvation structure. The local order is an important property for aqueous systems. Water is well-known as a tetrahedrally ordered fluid due to the highly directional hydrogen-bonding interactions. To analyze the local order, the following procedure is employed here: (i) for a given target molecule (O*H[−] for hydroxide solutions or H₂O* for pure water) all the hydrogens (H_d) whose closest intermolecular oxygen is O* in the system are located; (ii) the O*...H_d distance and the O*...H_dO_d angle are used to construct the first two-dimensional histogram, $P(r_{O^*H_d}, \cos\theta_{O^*H_dO_d})$; (iii) the O*...O_d distance and the H'O*...O_d angle are used to construct the second two-dimensional histogram $P(r_{O^*O_d}, \theta_{H'O^*O_d})$.

Compared in Figure 7 are $P(r_{O^*H_d}, \cos\theta_{O^*H_dO_d})$ for pure water and the various hydroxide solutions. For all systems, these histograms are essentially populated in a very small region centered around the preferred linear hydrogen-bond geometry. Compared to pure water, the distributions for the hydroxide solutions shift to significantly shorter distances (up to 0.2 Å for low concentration solutions). In addition, they are narrower in the angular axis, showing that OH[−] exerts a stronger directional force on its neighboring hydrogens. With an increase of the concentration, the distributions move to slightly larger distances. They also tail along the angular axis at the highest concentration for both NaOH and KOH systems. The distributions show little dependence on the counterion.

Different from $P(r_{O^*H_d}, \cos\theta_{O^*H_dO_d})$, the $P(r_{O^*O_d}, \theta_{H'O^*O_d})$ distributions are much broader, particularly along the angular axis (see Figure 8). While again only one region is prominent for water, an additional domain appears for the hydroxide at an unusually large $\theta_{H'O^*O_d}$ angle (around 180°, far away from the tetrahedral angle). This feature is especially clear for the 1.5 M NaOH solution and it is more noticeable for the NaOH systems than the KOH. Careful examination of these distributions also reveals that the primary region for the hydroxide is not centered around the tetrahedral angle as in pure water but at a slightly lower value. In addition, a small tilting of the contours is

observed for the hydroxide, showing a correlation between the $\theta_{H'O^*O_d}$ angle and the $r_{O^*O_d}$ distance (i.e., smaller $\theta_{H'O^*O_d}$ at larger $r_{O^*O_d}$). This tilting appears to shift the overall distributions to significantly shorter distances compared to pure water.

From the distributions shown in Figures 7 and 8, a molecule is determined to belong to the first solvation shell (FSS) of an OH[−] if $r_{OO} \leq 3.3$ Å and one of the hydrogens (either from this molecule or the OH[−]) satisfies $r_{OH} \leq 2.5$ Å and $\cos\theta_{OHO} \leq -0.5$. Plotted in Figure 9 are the number distributions of the FSS molecules. For comparison, the number distribution of the FSS molecules around H₂O was also analyzed for the pure water system using the same criteria (shown in Figure 9). It is clear that water prefers four neighbors in its first solvation shell, resulting in a simple and sharp distribution. In contrast, a much broader distribution is observed for OH[−], which extends to larger numbers (e.g., 5 and 6). In addition, the distribution appears to depend on both concentration and counterion. For example, the results on the NaOH systems show a clear shift of the distribution to smaller numbers with an increase of the concentration, whereas this is not so obvious for the KOH system. Also compared to NaOH, the KOH distribution moves to larger numbers at low concentrations but an opposite trend is observed at high concentrations, which is consistent with the number integral results and is due to the aforementioned reason.

By definition, the FSS molecules can be grouped into two categories: one bounded by the hydrogen of OH[−] (HFSS) and the other by its oxygen (OFSS). Considering that OH[−] has one hydrogen, which is only weakly hydrogen-bonded to other oxygens, most of the FSS molecules belong to the second category. Plotted in Figure 10 are the number distributions of the OFSS molecules. These distributions exhibit concentration and counterion dependencies similar to those plotted in Figure 9. As expected, 2 is the most probable number for water. For OH[−], however, a most probable number of 4 is observed for all hydroxide systems and 3 and 5 are the next most probable numbers.

We analyzed separately the spatial distribution functions (SDF) for those three types of OH[−] ions that have 3, 4, or 5 OFSS molecules, respectively (referred to as 3-, 4-, and 5-OFSS configurations). In the SDF analysis, the OH axis of the OH[−] ion is chosen as one of the reference axes. One of the OFSS

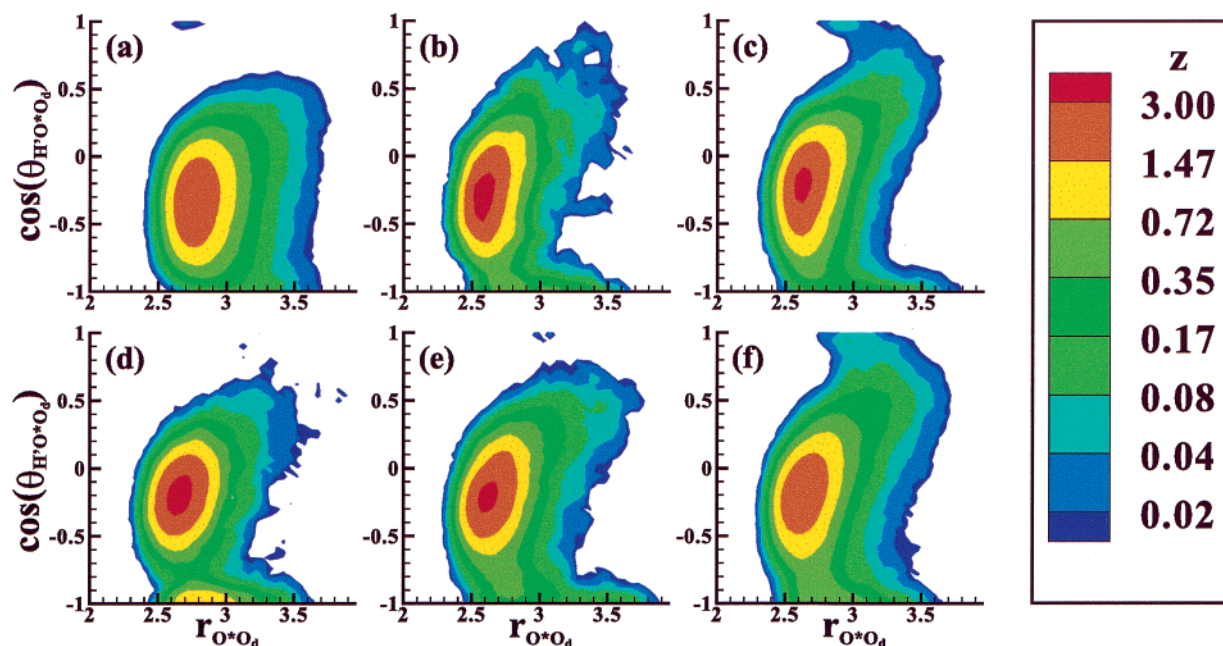


Figure 8. Contours of the two-dimensional distribution function of the O^{*}...O_d distance and of the cosine of the H'O^{*}...O_d angle calculated for pure water (panel a), KOH at 1.3 M (panel b) and 14 M (panel c), NaOH at 1.5 M (panel d), 4.5 M (panel e), and 15 M (panel f).

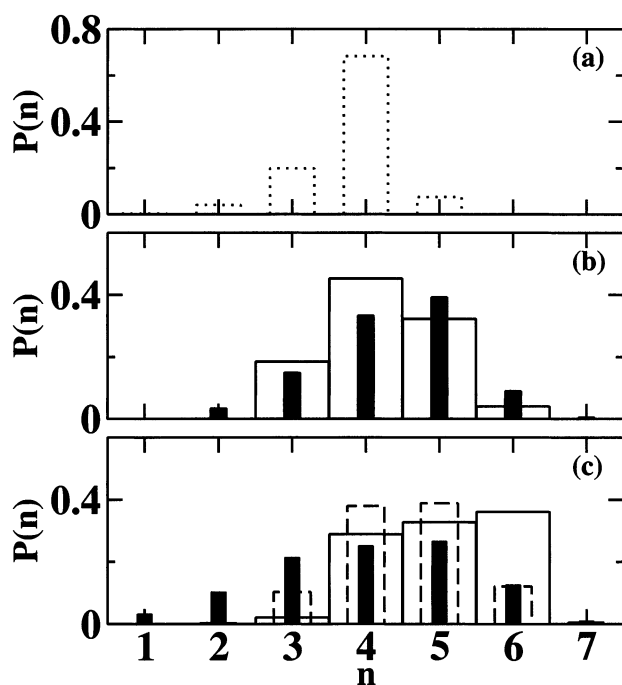


Figure 9. Number distributions of the first solvation shell molecules around water/OH⁻ calculated for (a) pure water, (b) KOH at 1.4 M (solid bar) and 14 M (filled bar), and (c) NaOH at 1.3 M (solid bar), 4.5 M (dashed bar), and 15 M (filled bar).

molecules, excluding the one which has the largest $\theta_{\text{H'O}^*\text{O}_d}$ angle, is selected to form the other reference axis. Interestingly, we found that each of them corresponds to a different picture shown in Figure 11. In the 3- or 4-OFSS configurations, the OFSS molecules are roughly evenly distributed in a plane perpendicular to the OH axis. In the 5-OFSS configurations, however, one of them is coordinated with the oxygen along the OH axis and the rest are distributed in a way similar to the 4-OFSS configurations. Averaging over the three types of configurations produces the same set of pictures, except for the 15 M NaOH solution, for which the SDF averaged over all 3-OFSS configurations turns out to be close to the 4-OFSS

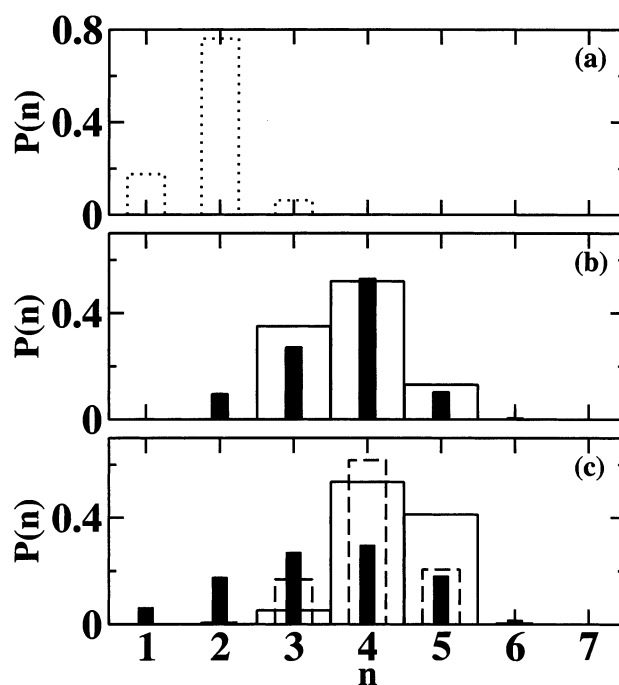


Figure 10. Number distributions of the oxygen-bound first solvation shell molecules around water/OH⁻. Symbols as in Figure 9.

configurations. This could be due to the fact that for this system, most of the 3-OFSS configurations were generated from a 4-OFSS configuration through a temporary leaving of a molecule from the solvation shell. For the same reason, it was found that the 2-OFSS configurations paint a picture similar to that of the normal 3-OFSS one.

Furthermore, the distribution of the $\theta_{\text{H'O}^*\text{O}_d}$ angle was calculated separately for these 3-, 4-, and 5-OFSS configurations. The results were plotted in Figure 12 as well as those for pure water. For all cases, except the 3-OFSS configurations obtained from the 1.3 M KOH solution, the distribution is displaced to the left with respect to the water distribution. In addition, this shift is enhanced with the increase in the number of neighbors, particularly for the low-concentration systems. For the 5-OFSS

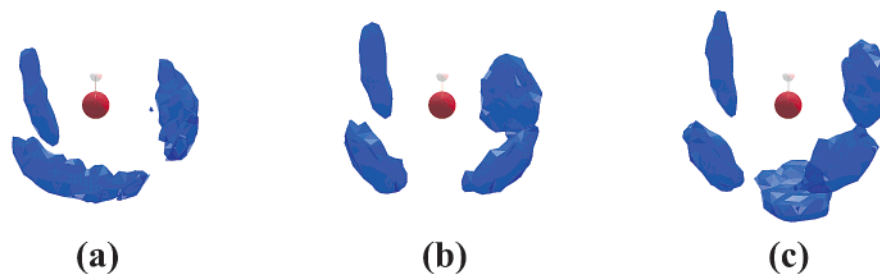


Figure 11. Isosurface of spatial distribution of water oxygen around OH^- at a density value of 0.15 \AA^{-3} . Panels a, b, and c are for OH^- ions that have 3, 4, or 5 oxygen-bound first solvation shell molecules, respectively.

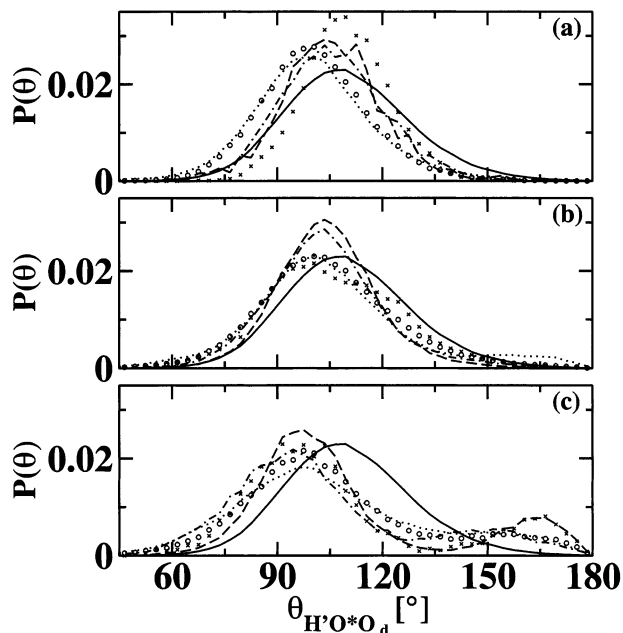


Figure 12. Distributions of the $\theta_{\text{H}'\text{O}^*\text{O}_d}$ angle for the oxygen-bound first solvation shell molecules around water/ OH^- . Panels a, b, and c are for OH^- ions that have 3, 4, or 5 oxygen-bound first solvation shell molecules, respectively. The following symbols are used for each system: solid lines (water), dashed lines (1.5 M NaOH), dashed–dotted lines (4.5 M NaOH), dotted lines (15 M NaOH), crosses (1.3 M KOH), and circles (14 M KOH).

configurations, the dominant peak appears at around 95° , which is significantly below the tetrahedral angle (109.5°). Also, a second peak appears at around 160° , contributed by the one neighbor positioned roughly at the bottom of OH^- (see Figure 11c). The differences between the KOH and NaOH systems are more appreciable at lower concentrations. For example, in the 3-OFSS case, the distributions of the low-concentration NaOH systems shift slightly to the left compared to that of the 1.3 M KOH solution, but both show a peak position around 109° , showing a preference for a tetrahedral geometry. The broadness of these distributions implies an orientational asymmetry of the solvation shell around OH^- . Analysis on the $r_{\text{O}^*\text{O}_d}$ distances also indicates that the solvation shell is asymmetric from a different perspective. The standard error of mean was analyzed for the set of $r_{\text{O}^*\text{O}_d}$ distances for each individual configuration. The average value is around 0.07 \AA for all three different configurations, except for the 3-OFSS configurations in the 1.3 M KOH solution which is noticeably smaller (0.05 \AA).

C. Solvation Structures and Proton-Transfer Mechanisms of OH^- . It is evident from the above structural analysis that three dominant solvation structures are present for OH^- in both KOH and NaOH systems over all concentrations. They are $\text{OH}^-(\text{H}_2\text{O})_3$, $\text{OH}^-(\text{H}_2\text{O})_4$, and $\text{OH}^-(\text{H}_2\text{O})_5$. The geometry of

these complexes can be characterized by the spatial distribution functions shown in Figure 11 and the angle distributions shown in Figure 12. Their concentrations can be roughly estimated based on the number distributions shown in Figure 10. Visual inspection of the configurations also demonstrates that other complexes exist in these solutions but they are relatively more transient. For example, a different penta-solvated complex (with five water molecules coordinated to OH^- roughly in the same plane) was found for these systems. H_3O_2^- is another example.

These findings are apparently at odds with the spectroscopic interpretations,²⁰ which suggest that H_3O_2^- is the dominant solvation structure. In addition, they differ somewhat from those obtained in the previous ab initio study by Tuckerman et al.^{1,11} on a system with OH^- in 31 H_2O without the counterion. In their study, the planar $\text{OH}^-(\text{H}_2\text{O})_4$ (see Figure 1c) was reported to be the only dominant solvation structure. It was also observed to form transient hydrogen bonds with a water molecule below the plane. In contrast, we found that this type of hydrogen bond is very stable in the presence of counterions (in particular, Na^+). In addition, the presence of K^+ or an increase in the concentration enhances substantially the frequency of occurrence for the $\text{OH}^-(\text{H}_2\text{O})_3$ complex and it can no longer be regarded as a transient complex at those conditions. All these differences clearly point to the significant influence of the counterion and the concentration on the relative stabilities of different solvated complexes. Indeed, further RDF analysis on individual OH^- configurations supports this.

Plotted in Figure 13 are the $\text{O}^*-\text{K}/\text{Na}$ RDFs and/or number integrals for the 3-, 4-, and 5-OFSS configurations. For the two high-concentration solutions, the results of the 2-OFSS configurations are also shown. An interesting observation from this figure is that for all systems, the higher the number of the OFSS molecules around an OH^- , the less likely for the counterions to be present in its first solvation shell but the more likely for them to be in the second solvation shell. It is evident that most of the $\text{OH}^-(\text{H}_2\text{O})_3$ complexes are stabilized by having direct contacts with counterions (on average, an $\text{OH}^-(\text{H}_2\text{O})_3$ complex is surrounded by up to two counterions in the high concentration solutions). Thus the counterion- and concentration dependencies of the frequency of this complex can be simply explained as follows. At low concentrations the higher probability to observe this complex in KOH than NaOH is due to the fact that K^+ is more likely to form a contact ion pair with OH^- than Na^+ . Compared to low concentrations, the more frequent appearance of this complex at high concentrations is due to the presence of significantly larger number of contact ion pairs. In a similar way, we could explain the counterion- and concentration dependencies of the frequency of the $\text{OH}^-(\text{H}_2\text{O})_5$ complex. This complex appears to be stabilized by the presence of a counterion in the second solvation shell (a solvent separated ion pair). Na^+ particularly prefers this position compared to K^+ , probably because the size of Na^+ and its octahedral coordination pattern

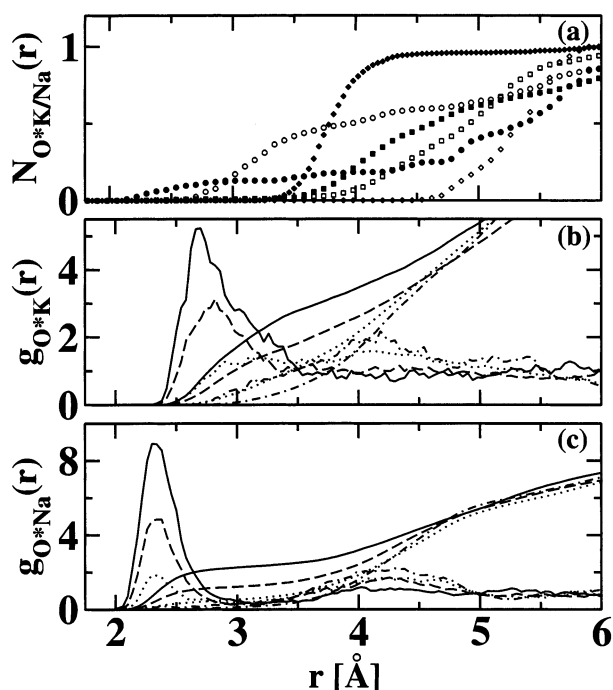


Figure 13. O*–Na⁺ or O*–K⁺ radial distribution functions and their corresponding number integrals for OH[−] ions that have 2 (solid lines), 3 (circles and dashed lines), 4 (squares and dotted), or 5 (diamonds and dashed–dotted lines) oxygen-bound first solvation shell molecules. Panel a is for the 1.3 M KOH (open symbols) and 1.5 M NaOH (filled symbols). Panels b and c are for the 14 M KOH and 15 M NaOH, respectively. For the two low-concentration systems, the radial distribution functions were not shown for clarity.

(not shown here) are compatible with the geometry of the OH[−](H₂O)₅ complex. In the 1.5 M NaOH solution, the number integral results (near 0 at 3.2 Å but close to 1 at 4.5 Å) indicate that the majority of the OH[−](H₂O)₅ complexes are involved in a contact pair with a solvated Na⁺. The less frequent appearances of this complex at higher concentrations could be due to the lower water/ion ratio and the more direct contacts between OH[−] and the counterions.

Interestingly for the systems investigated here, both the concentration and the counterions seem to alter mostly the fraction of the OH[−](H₂O)₃ and OH[−](H₂O)₅ (probably because K⁺ prefers a contact ion pair whereas Na⁺ prefers a solvent separated ion pair). OH[−](H₂O)₄ remains as the most populated species. However, gas-phase *ab initio* calculations^{22,23} indicate that the tetrahedral tri-solvated complex is more stable than the planar tetra-solvated complex. This might suggest that the bulk solvation environment and the thermal fluctuations also affect the stabilities of these complexes.

To explore the role of these complexes in the proton-transfer event, the probability distributions of the 3-, 4-, and 5-OFSS configurations were plotted against both δ_{\min} and $\theta_{\text{H}^*\text{O}^*\text{O}_d}$ (see Figure 14). δ_{\min} is selected as one of the axes in the construction of these two-dimensional histograms because it is often regarded as a convenient choice for the proton-transfer coordinate (i.e., proton transfer happens with the decrease of δ_{\min}). $\theta_{\text{H}^*\text{O}^*\text{O}_d}$ is used to examine the possible geometry change along the main proton-transfer coordinate δ_{\min} . As shown by Figure 14, for all systems, both OH[−](H₂O)₃ and OH[−](H₂O)₄ have nonzero probabilities at $\delta_{\min} = 0$ whereas OH[−](H₂O)₅ is nearly completely depleted at that spot. An immediate conclusion from this is that both OH[−](H₂O)₃ and OH[−](H₂O)₄ are proton-transfer active while OH[−](H₂O)₅ is not. Also in the 1.5 M NaOH solution, the flat distributions of the 3-OFSS configurations

along δ_{\min} suggest that proton transfer is nearly barrierless in this case. Both the presence of K⁺ and the increase of the concentration shift the distributions of the 3-OFSS configurations to larger δ_{\min} , which leads to a stable region and a small barrier for proton transfer. In contrast, for all systems a very stable region exists at large δ_{\min} values for the 4-OFSS configurations, whereas fewer of them are observed at $\delta_{\min} = 0$. Correspondingly, the proton-transfer barriers are much higher compared to the 3-OFSS configurations. In addition, the distributions change from being dominated by 4-OFSS configurations to 3-OFSS configurations with the decrease of δ_{\min} , which implies that a change of the complex type might happen during the proton-transfer event.

It should be noted that a small adjustment to a more tetrahedral-like geometry also occurs during the proton-transfer process. This is reflected by the $\theta_{\text{H}^*\text{O}^*\text{O}_d}$ distributions, which are centered around the tetrahedral angle at small δ_{\min} values, whereas the distributions are broadened along the $\theta_{\text{H}^*\text{O}^*\text{O}_d}$ angle at high δ_{\min} values. In particular, the distributions were split into two regions along the θ axis for the OH[−](H₂O)₅ configurations. For both 4-OFSS and 5-OFSS configurations, the primary region was centered at a value below the tetrahedral angle. This is also true for the 3-OFSS configurations in the concentrated systems (see the small tilting of the distributions in Figure 14).

Figure 15 paints a similar picture regarding the proton-transfer activity of these species, in which a recording of the proton-transfer events (by a function $P(t)$, $P(t) = 1$ if there is a proton-transfer event or 0 otherwise) is shown in parallel with the time evolutions of the O*...K⁺ separation and the number of OFSS molecules. It is clear that proton transfer happens most frequently when OH[−] is in the 3-OFSS configuration while it completely terminates at the 5-OFSS configuration. Also illustrated in these plots is the fact that the counterion plays a double-sided role in proton transfer. It activates proton transfer by stabilizing the 3-OFSS configurations through direct contact with OH[−]. For example, a few proton transfers were even observed to transfer from a 4-OFSS configuration to a 3-OFSS configuration, mostly due to the presence of a counterion in the first solvation shell of a newly created OH[−]. Stabilization of these complexes (by the counterion), on the other hand, can also lead to a termination of proton transfer. Particularly in the NaOH systems (not shown here), the counterion stabilizes the 5-OFSS configurations and stops the proton transfer completely.

In the study by Tuckerman et al.^{1,11} it was also determined that OH[−](H₂O)₃ is the most active species in proton transfer. Without counterions in their system, it was concluded that OH[−](H₂O)₄ behaves as a terminator of proton transfer, and a first solvation shell structural reorganization (i.e., from OH[−](H₂O)₄ to OH[−](H₂O)₃) needs to take place for proton transfer. In contrast, we have shown above that this type of structural reorganization is a prerequisite only for OH[−](H₂O)₅ but not for OH[−](H₂O)₄ when counterions are present. However, the major picture remains, that is, the transport mechanism of the hydroxide ion differs from that of proton and it involves the first solvation shell structural reorganization process.

Figure 16 is a view of proton transfer from another perspective, where the δ_{\min} coordinate and the oxygen–oxygen distance were used to construct the contour plots. From the tilting of these distributions, it is clear that during the proton-transfer process, there is a concurrent shrinkage of the oxygen–oxygen distance (especially the one neighbor with the most active proton). The counterion affects little the distributions along the oxygen–oxygen distance axis whereas both the increase of the

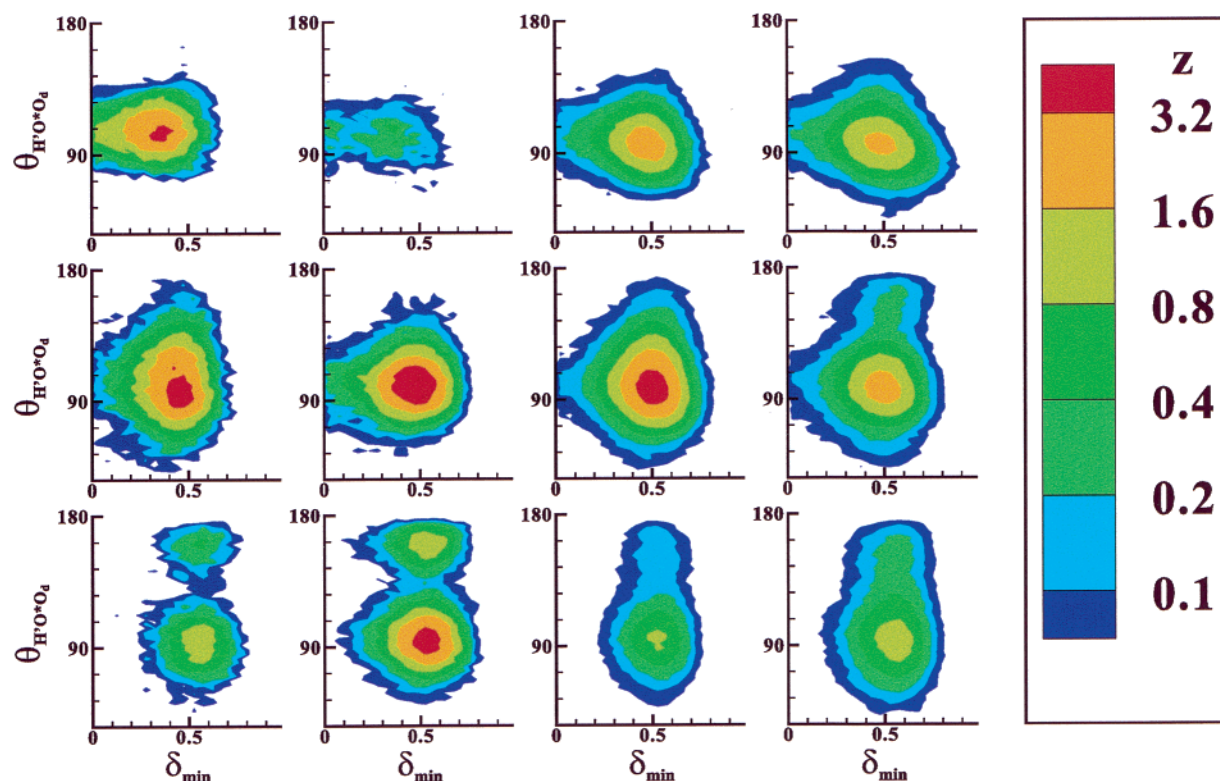


Figure 14. Contours of the two-dimensional distribution function of the δ_{\min} distance and the $\theta_{\text{H}_2\text{O}^*\text{O}_d}$ angle for all the oxygen-bound first solvation shell molecules around OH^- . The top, middle, and bottom four panels are for OH^- ions that have 3, 4, or 5 oxygen-bound first solvation shell molecules, respectively. The results for the 1.3M KOH, 1.5M NaOH, 14M KOH, and 15M NaOH are displayed from left to right.

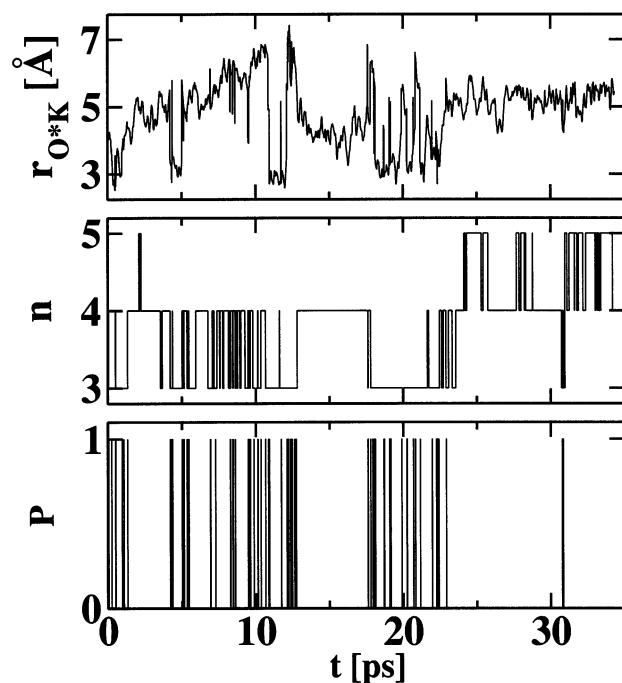


Figure 15. Time evolution of the $\text{O}^*\cdots\text{K}^+$ separation, the number of oxygen-bound first solvation shell molecules around OH^- , and P function indicating proton-transfer event (see text) in the 1.3 M KOH solution.

concentration and the increase of the number of OFSS molecules broaden the distributions to larger oxygen–oxygen separations. In particular, for most of the 3-OFSS configurations in the dilute systems, all three neighbors show an oxygen–oxygen separation with OH^- below 3 Å, indicating that they are all tightly hydrogen bonded to OH^- .

D. Vibrational Spectra. While the microscopic-level structures described above are very rich, they disagree with the structural models inferred previously from spectroscopic experiments²⁰ on concentrated systems. Thus, it is imperative for us to show whether these simulations can reproduce spectroscopic data.

Shown in Figure 17 are the velocity autocorrelation power spectra for all the deuterium atoms. From the figure it appears that the OH stretch of the KOH systems shifts to lower frequencies by about 40 wavenumbers compared to the NaOH systems, but actually this is due to the use of different plane wave basis set cutoffs. An additional short simulation on one of the NaOH systems using 70 Ry instead of 80 Ry confirmed this. Excluding this small systematic shift, the spectra for the low-concentration solutions (1.5 M NaOH and 1.3 M KOH) are very close to each other and also to that of pure water. In contrast, at high concentrations, new spectroscopic features appear that are very distinct from those of pure water. For both KOH and NaOH systems, while the water bending motion is essentially undisturbed by the presence of hydroxide, there is a significant broadening of the O–D stretch and also a large shift of the libration band to larger wavenumbers. In addition, a spike appears at 2550 cm^{-1} for NaOH and 2510 cm^{-1} for KOH. Remarkably, these features resemble well the basic characteristics of the experimental spectra at similar concentrations (notice in the experimental Raman spectrum a comparable broadening of the O–D or O–H stretch and a spike at 2660 cm^{-1} for NaOD and 3600 cm^{-1} for KOH). From an analysis of the spectrum of individual hydrogen atoms, it was found that the free O–D stretch of OD^- (which is only involved in a weak hydrogen bond as demonstrated above) is responsible for the appearance of this spike. Those hydrogens that are strongly hydrogen bonded to OD^- are responsible for many of the other features.

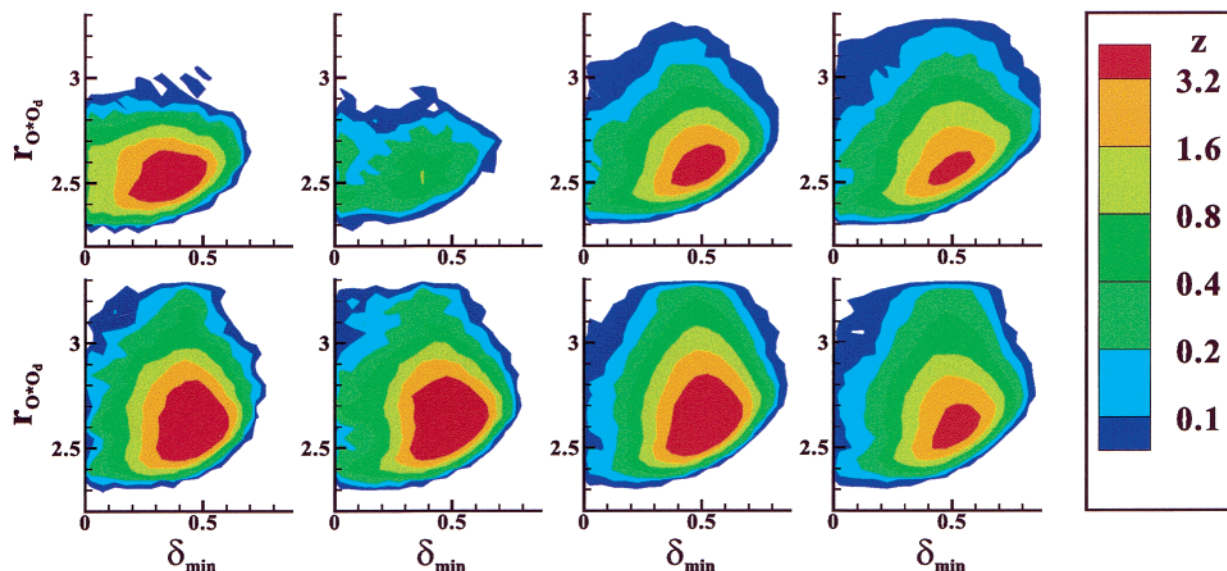


Figure 16. Contours of the two-dimensional distribution function of the δ_{\min} and the O^*O_d distance for all the oxygen-bound first solvation shell molecules around OH^- . The top and bottom four panels are for OH^- ions that have 3 or 4 oxygen-bound first solvation shell molecules, respectively. The results for the 1.3 M KOH, 1.5 M NaOH, 14 M KOH, and 15 M NaOH are displayed from left to right.

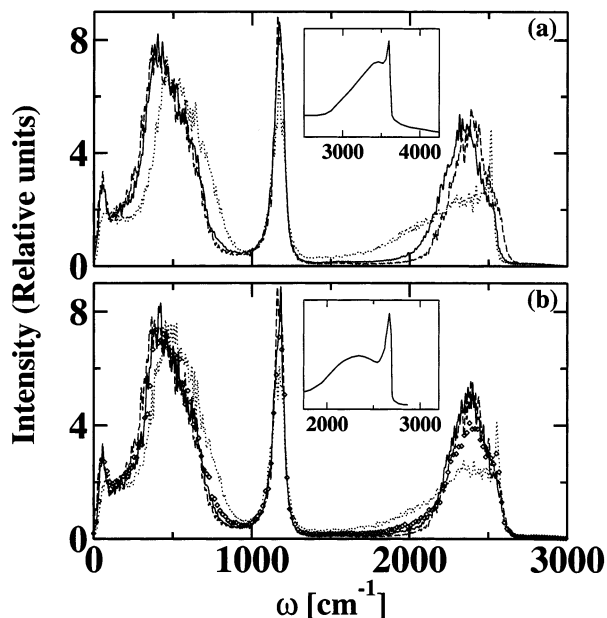


Figure 17. Comparison of power spectra derived from deuterium velocity autocorrelation functions for pure water (dashed lines in both panels a and b), KOD (panel a) at 1.3 M (solid line) and 14 M (dotted line), and NaOD (panel b) at 1.5 M (solid line), 4.5 M (diamonds), and 15 M (dotted line). The experimental Raman spectra²⁰ for 48.1% KOH and 43.4% NaOD are shown as an inset in panels a and b, respectively.

It should be kept in mind that the power spectra calculated above in principle contain both IR and Raman features. To analyze the modes that are only IR active, the dipole-moment auto-correlation function was used.^{32,45} The IR absorption coefficient $\alpha(\omega)$ was calculated as follows,³²

$$\alpha(\omega) = \frac{4\pi\tau\text{tanh}(\beta\hbar\omega/2)}{3\hbar n(\omega)cV} \times \int_{-\infty}^{\infty} dt \exp(-i\omega t) \langle \mathbf{M}(t) \cdot \mathbf{M}(0) \rangle \quad (1)$$

where V is the volume, $\beta = 1/k_B T$ is the inverse temperature, $n(\omega)$ is the refractive index, c is the speed of light in vacuum, \mathbf{M} is the total dipole moment (ionic plus electronic) of the

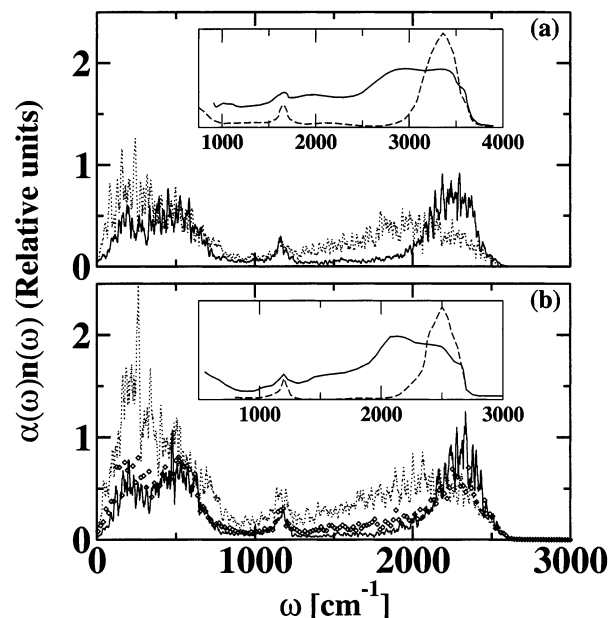


Figure 18. Comparison of IR spectra. Symbols as in Figure 17. The experimental IR spectra for 48.1% KOH and 43.4% NaOD (solid lines) together with the experimental spectra²⁰ for the corresponding water systems (dashed lines) are shown as an inset in panels a and b, respectively.

sample, and the angular brackets denote an ensemble average. Since the Berry phase scheme was used for the calculation, the dipole moment had to be corrected by a constant offset related to lattice translations.^{46,47} To reduce the computational noise, following ref 45, the Fourier transformation was performed on the autocorrelation function of the time derivative of the dipole moment (computed by means of finite differences) instead of the dipole moment using the relation,

$$\int_{-\infty}^{\infty} dt \exp(-i\omega t) \langle \dot{\mathbf{M}}(t) \cdot \dot{\mathbf{M}}(0) \rangle = \omega^2 \int_{-\infty}^{\infty} dt \exp(-i\omega t) \langle \mathbf{M}(t) \cdot \mathbf{M}(0) \rangle \quad (2)$$

A second-order Savitzky–Golay smoothing procedure was applied afterward.⁴⁸

Plotted in Figure 18 are the IR spectra for the different systems investigated here (unfortunately we did not collect dipole dynamics in the simulation on pure water, but readers can refer to ref 32 for the IR spectrum calculated for pure water). For comparison, the experimental IR spectra for pure water and concentrated systems were also shown.²⁰ The major features in these IR spectra are very similar to those of the deuterium spectra: the bending mode remains undisturbed whereas the O–D stretch is significantly broadened, which is consistent with the experimental IR spectra. Also in agreement with the experiments, the spike observed in the deuterium spectra for the concentrated systems is barely seen in these IR spectra. It was mentioned before that the experiments interpreted this IR inactivity as a formation of symmetric H_3O_2^- complex.²⁰ However, it was found in the present simulations on both NaOH and KOH systems that H_3O_2^- only appears as a transient complex that has to be visited in the proton transfer process. Probably repeated proton transfer (back and forth between two neighboring oxygens) is responsible for the reduced IR activity of the free O–D stretch of OD^- . It should be also noted that at low concentrations, the IR spectra are very similar to those of pure water reported in ref 32.

4. Conclusions

The CPMD simulations reported herein are able to reproduce the experimentally observed changes in the structural and dynamical properties of water with the addition of hydroxide. For example, the normal tetrahedral coordination of water was found completely missing at high concentrations for both NaOH and KOH systems, consistent with the interpretations from the recent neutron diffraction experiments. Also, analysis on the velocity autocorrelation power spectra reveal several distinct spectroscopic features for hydroxide systems observed by the spectroscopic experiments, including a “free” O–H stretch and a broadening of the normal water O–H stretch. Further IR calculations surprisingly confirm the reduced activity of this “free” O–H stretch.

Extensive analysis has demonstrated that the structural and dynamical behavior of the hydroxide system is inextricably linked to the strong OH^- ion–water interactions and the formation of various complexes. Three dominant complexes are present: $\text{OH}^-(\text{H}_2\text{O})_3$, $\text{OH}^-(\text{H}_2\text{O})_4$, and $\text{OH}^-(\text{H}_2\text{O})_5$. The distribution among these complexes is dependent upon the concentration and the counterion. For example, K^+ stabilizes $\text{OH}^-(\text{H}_2\text{O})_3$ by having direct contacts with OH^- , whereas Na^+ stabilizes $\text{OH}^-(\text{H}_2\text{O})_5$ by forming a solvent separated ion pair. Concentration influences the occurrence of these complexes by changing the water/ion ratio and the frequencies of these contact pairs. These results differ somewhat from those shown by Tuckerman et al. who studied a system with 1 OH^- in 31 H_2O without the counterion. However, the present investigation supports their view that the transport mechanism of the hydroxide ion is different from that of the proton.

Finally, it should be pointed out that Zhu and Tuckerman recently carried out an independent CPMD investigation on the KOH solutions.⁴⁹ The structural and dynamical results obtained therein are very similar to ours. In both studies relatively small system sizes are employed. However, we would like to argue that the finite-size effects may influence the quantitative details of the behavior of the hydroxide solutions but not the qualitative picture.⁵⁰ Investigations on larger system sizes are necessary to clarify this point but are beyond the current capability of the CPMD methodology.

Acknowledgment. We thank Prof. Fabio Bruni for sharing the experimental work with us and both Mark Tuckerman and Simone Raugei for many stimulating discussions. We also thank

Preston Moore for help with the visualization of the spatial distribution functions. This research was supported by the National Science Foundation under CHE-0205146. Computer resources were provided partly by the Pittsburgh Supercomputing Center through NPACI.

References and Notes

- (1) Tuckerman, M. E.; Laasonen, K.; Sprik, M.; Parrinello, M. *J. Chem. Phys.* **1995**, *103*, 150.
- (2) Agmon, N. *Chem. Phys. Lett.* **1995**, *244*, 456.
- (3) Marx, D.; Tuckerman, M. E.; Hutter, J.; Parrinello, M. *Nature* **1999**, *397*, 601.
- (4) Hynes, J. T. *Nature* **1999**, *397*, 565.
- (5) Marx, D.; Tuckerman, M. E.; Parrinello, M. *J. Phys.: Condens. Matter* **2000**, *12*, A153.
- (6) Vuilleumier, R.; Borgis, D. *J. Chem. Phys.* **1999**, *111*, 4251.
- (7) Day, T. J. F.; Schmitt, U. W.; Voth, G. A. *J. Am. Chem. Soc.* **2000**, *122*, 12027.
- (8) Zatschina, P. N. *J. Struct. Chem.* **1969**, *10*, 200.
- (9) Tuñón, I.; Rinaldi, D.; Ruiz-López, M. F.; Rivail, J. L. *J. Phys. Chem.* **1995**, *99*, 3798.
- (10) Muller, R. P.; Warshel, A. *J. Phys. Chem.* **1995**, *99*, 17516.
- (11) Tuckerman, M. E.; Marx, D.; Parrinello, M. *Nature* **2002**, *417*, 925.
- (12) Agmon, N. *Chem. Phys. Lett.* **2000**, *319*, 247.
- (13) Danneel, H. Z. *Elektrochem.* **1905**, *16*, 249.
- (14) Hückel, E. Z. *Elektrochem.* **1928**, *34*, 546.
- (15) Meot-Ner, M.; Speller, C. V. *J. Phys. Chem.* **1986**, *90*, 6616.
- (16) Busing, W. R.; Hornig, D. F. *J. Chem. Phys.* **1961**, *65*, 284.
- (17) Zatschina, P. N. *J. Struct. Chem.* **1971**, *12*, 894.
- (18) Schiöberg, D.; Zundel, G. *J. Chem. Soc., Faraday Trans. 2* **1973**, *69*, 771.
- (19) Librovich, N. B.; Sakun, V. P.; Sokolov, N. D. *Chem. Phys.* **1979**, *39*, 351.
- (20) Librovich, N. B.; Maiorov, V. D. *Russ. J. Phys. Chem.* **1982**, *56*, 380.
- (21) Buchner, R.; Hefter, G.; May, P. M.; Sipos, P. *J. Phys. Chem. B* **1999**, *103*, 11186.
- (22) Grimm, A. R.; Bacskey, G. B.; Haymet, A. D. *J. Mol. Phys.* **1995**, *86*, 369.
- (23) Novoa, J. J.; Mota, F.; delValle, C. P.; Planas, M. *J. Phys. Chem. A* **1997**, *101*, 7842.
- (24) Amo, Y.; Tominaga, Y. *J. Raman Spec.* **2000**, *31*, 547.
- (25) Bruni, F.; Ricci, M. A.; Soper, A. K. *J. Chem. Phys.* **2001**, *114*, 8056.
- (26) Car, R.; Parrinello, M. *Phys. Rev. Lett.* **1985**, *55*, 2471.
- (27) CPMD version 3.4, Hutter, J.; Alavi, A.; Deutsch, T.; Bernasconi, M.; Goedecker, S.; Marx, D.; Tuckerman, M. E.; Parrinello, M. MPI für Festkörperforschung and IBM Research Laboratory, Stuttgart and Zürich, 1995–2000.
- (28) Becke, A. D. *Phys. Rev. A* **1988**, *38*, 3098.
- (29) Lee, C.; Yang, W.; Parr, R. C. *Phys. Rev. B* **1988**, *37*, 785.
- (30) Ramaniah, L. M.; Bernasconi, M.; Parrinello, M. *J. Chem. Phys.* **1999**, *111*, 1587.
- (31) Sprik, M.; Hutter, J.; Parrinello, M. *J. Chem. Phys.* **1996**, *105*, 1142.
- (32) Silvestrelli, P. L.; Bernasconi, M.; Parrinello, M. *Chem. Phys. Lett.* **1997**, *277*, 478.
- (33) Troullier, N.; Martins, J. L. *Phys. Rev. B* **1991**, *43*, 1993.
- (34) Kleinman, L.; Bylander, D. M. *Phys. Rev. Lett.* **1982**, *48*, 1425.
- (35) Laasonen, K.; Sprik, M.; Parrinello, M. *J. Chem. Phys.* **1993**, *99*, 9080.
- (36) Lide, D. A. *CRC Handbook of Chemistry and Physics*; CRC Press: Boca Raton, 1991.
- (37) Pitis, R.; Huckaby, D. A. *Physica A* **1996**, *232*, 702.
- (38) Kuhs, W. F.; Finney, J. L.; Vettier, C.; Bliss, D. V. *J. Chem. Phys.* **1984**, *81*, 3612.
- (39) Nosé, S. *J. Chem. Phys.* **1984**, *81*, 511.
- (40) Nosé, S. *Mol. Phys.* **1984**, *52*, 255.
- (41) Hoover, W. G. *Phys. Rev. A* **1985**, *31*, 1695.
- (42) Martyna, G. J.; Tuckerman, M. E.; Klein, M. L. *J. Chem. Phys.* **1992**, *97*, 2635.
- (43) Chen, B.; Park, J. M.; Ivanov, I.; Tabacchi, G.; Klein, M. L.; Parrinello, M. *J. Am. Chem. Soc.* **2002**, *124*, 8534.
- (44) Tuckerman, M. E.; Ungar, P. J.; von Rosenfeld, T.; Klein, M. L. *J. Phys. Chem.* **1996**, *100*, 12878.
- (45) Debernardi, A.; Bernasconi, M.; Cardona, M.; Parrinello, M. *Appl. Phys. Lett.* **1997**, *71*, 2692.
- (46) King-Smith, R. D.; Vanderbilt, D. *Phys. Rev. B* **1993**, *47*, 1651.
- (47) Resta, R. *Rev. Mod. Phys.* **1994**, *66*, 899.
- (48) Savitzky, A.; Golay, M. J. E. *Anal. Chem.* **1964**, *36*, 1627.
- (49) Zhu, Z.; Tuckerman, M. E. *J. Phys. Chem. B* **2002**, *106*, 8009.
- (50) Klein, M. L. *Science* **2001**, *291*, 2106.